arXiv:astro-ph/0608606v2 21 Sep 2006

Searching for a Stochastic Background of Gravitational Waves with LIGO

B. Abbott[12], R. Abbott[12], R. Adhikari[12], J. Agresti[12], P. Ajith[2], B. Allen[42], R. Amin[16], S. B. Anderson[12], W. G. Anderson[42], M. Araya[12], H. Armandula[12], M. Ashley[3], S Aston[34], C. Aulbert[1], S. Babak[1], S. Ballmer[13], B. C. Barish[12], C. Barker[14], D. Barker[14], B. Barr[36], P. Barriga[41], M. A. Barton[12], K. Bayer[13], K. Belczynski[22], J. Betzwieser[13], P. Beyersdorf[26], B. Bhawal[12], I. A. Bilenko[19], G. Billingsley[12], E. Black[12], K. Blackburn[12], L. Blackburn[13], D. Blair[41], B. Bland[14], L. Bogue[15], R. Bork[12], S. Bose[43], P. R. Brady[42], V. B. Braginsky[19], J. E. Brau[39], A. Brooks[33], D. A. Brown[12], A. Bullington[26], A. Bunkowski[2], A. Buonanno[37], R. Burman[41], D. Busby[12], R. L. Byer[26], L. Cadonati[13], G. Cagnoli[36], J. B. Camp[20], J. Cannizzo[20], K. Cannon[42], C. A. Cantley[36], J. Cao[13], L. Cardenas[12], M. M. Casey[36], C. Cepeda[12], P. Charlton[12], S. Chatterji[12], S. Chelkowski[2], Y. Chen[1], D. Chin[38], E. Chin[41], J. Chow[3], N. Christensen[7], T. Cokelaer[6], C. N. Colacino[34], R. Coldwell[35], D. Cook[14], T. Corbitt[13], D. Coward[41], D. Coyne[12], J. D. E. Creighton[42], T. D. Creighton[12], D. R. M. Crooks[36], A. M. Cruise[34], A. Cumming[36], C. Cutler[5], J. Dalrymple[27], E. D'Ambrosio[12], K. Danzmann[31,2], G. Davies[6], G. de Vine[3], D. DeBra[26], J. Degallaix[41], V. Dergachev[38], S. Desai[28], R. DeSalvo[12], S. Dhurandar[11], A. Di Credico[27], M. Díaz[29], J. Dickson[3], G. Diederichs[31], A. Dietz[16], E. E. Doomes[25], R. W. P. Drever[4], J.-C. Dumas[41], R. J. Dupuis[12], P. Ehrens[12], E. Elliffe[36], T. Etzel[12], M. Evans[12], T. Evans[15], S. Fairhurst[42], Y. Fan[41], M. M. Fejer[26], L. S. Finn[28], N. Fotopoulos[13], A. Franzen[31], K. Y. Franzen[35], R. E. Frey[39], T. Fricke[40], P. Fritschel[13], V. V. Frolov[15], M. Fyffe[15], J. Garofoli[14], I. Gholami[1], J. A. Giaime[16], S. Giampanis[40], K. Goda[13], E. Goetz[38], L. Goggin[12], G. González[16], S. Gossler[3], A. Grant[36], S. Gras[41], C. Gray[14], M. Gray[3], J. Greenhalgh[23], A. M. Gretarsson[9], D. Grimmett[12], R. Grosso[29], H. Grote[2], S. Grunewald[1], M. Guenther[14], R. Gustafson[38], B. Hage[31], C. Hanna[16], J. Hanson[15], C. Hardham[26], J. Harms[2], G. Harry[13], E. Harstad[39], T. Hayler[23], J. Heefner[12], I. S. Heng[36], A. Heptonstall[36], M. Heurs[31], M. Hewitson[2], S. Hild[31], N. Hindman[14], E. Hirose[27], D. Hoak[15], P. Hoang[12], D. Hosken[33], J. Hough[36], E. Howell[41], D. Hoyland[34], W. Hua[26], S. Huttner[36], D. Ingram[14], M. Ito[39], Y. Itoh[42], A. Ivanov[12], D. Jackrel[26], B. Johnson[14], W. W. Johnson[16], D. I. Jones[36], G. Jones[6], R. Jones[36], L. Ju[41], P. Kalmus[8], V. Kalogera[22], D. Kasprzyk[34], E. Katsavounidis[13], K. Kawabe[14], S. Kawamura[21], F. Kawazoe[21], W. Kells[12], F. Ya. Khalili[19], A. Khan[15], C. Kim[22], P. King[12], S. Klimenko[35], K. Kokeyama[21], V. Kondrashov[12], S. Koranda[42], D. Kozak[12], B. Krishnan[1], P. Kwee[31], P. K. Lam[3], M. Landry[14], B. Lantz[26], A. Lazzarini[12], B. Lee[41], M. Lei[12], V. Leonhardt[21], I. Leonor[39], K. Libbrecht[12], P. Lindquist[12], N. A. Lockerbie[34], M. Lormand[15], M. Lubinski[14], H. Lück[31,2], B. Machenschalk[1], M. MacInnis[13], M. Mageswaran[12], K. Mailand[12], M. Malec[31], V. Mandic[12], S. Márka[8], J. Markowitz[13], E. Maros[12], I. Martin[36], J. N. Marx[12],

K. Mason[13], L. Matone[8], N. Mavalvala[13], R. McCarthy[14], D. E. McClelland[3], S. C. McGuire[25], M. McHugh[18], K. McKenzie[3], J. W. C. McNabb[28], T. Meier[31], A. Melissinos[40], G. Mendell[14], R. A. Mercer[35], S. Meshkov[12], E. Messaritaki[42], C. J. Messenger[36], D. Meyers[12], E. Mikhailov[13], S. Mitra[11], V. P. Mitrofanov[19], G. Mitselmakher[35], R. Mittleman[13], O. Miyakawa[12], S. Mohanty[29], G. Moreno[14], K. Mossavi[2], C. MowLowry[3], A. Moylan[3], D. Mudge[33], G. Mueller[35], H. Müller-Ebhardt[2], S. Mukherjee[29], J. Munch[33], P. Murray[36], E. Myers[14], J. Myers[14], G. Newton[36], K. Numata[20], B. O'Reilly[15], R. O'Shaughnessy[22], D. J. Ottaway[13], H. Overmier[15], B. J. Owen[28], Y. Pan[5], M. A. Papa[1,42], V. Parameshwaraiah[14], M. Pedraza[12], S. Penn[10], M. Pitkin[36], M. V. Plissi[36], R. Prix[1], V. Quetschke[35], F. Raab[14], D. Rabeling[3], H. Radkins[14], R. Rahkola[39], M. Rakhmanov[28], K. Rawlins[13], S. Ray-Majumder[42], V. Re[34], H. Rehbein[2], S. Reid[36], D. H. Reitze[35], L. Ribichini[2], R. Riesen[15], K. Riles[38], B. Rivera[14], D. I. Robertson[36], N. A. Robertson[26,36], C. Robinson[6], S. Roddy[15], A. Rodriguez[16], A. M. Rogan[43], J. Rollins[8], J. D. Romano[6], J. Romie[15], R. Route[26], S. Rowan[36], A. Rüdiger[2], L. Ruet[13], P. Russell[12], K. Ryan[14], S. Sakata[21], M. Samidi[12], L. Sancho de la Jordana[32], V. Sandberg[14], V. Sannibale[12], S.Saraf[26], P. Sarin[13], B. S. Sathyaprakash[6], S. Sato[21], P. R. Saulson[27], R. Savage[14], S. Schediwy[41], R. Schilling[2], R. Schnabel[2], R. Schofield[39], B. F. Schutz[1,6], P. Schwinberg[14], S. M. Scott[3], S. E. Seader[43], A. C. Searle[3], B. Sears[12], F. Seifert[2], D. Sellers[15], A. S. Sengupta[6], P. Shawhan[12], B. Sheard[3], D. H. Shoemaker[13], A. Sibley[15], X. Siemens[42], D. Sigg[14], A. M. Sintes[32,1], B. Slagmolen[3], J. Slutsky[16], J. Smith[2], M. R. Smith[12], P. Sneddon[36], K. Somiya[2,1], C. Speake[34], O. Spjeld[15], K. A. Strain[36], D. M. Strom[39], A. Stuver[28], T. Summerscales[28], K. Sun[26], M. Sung[16], P. J. Sutton[12], D. B. Tanner[35], M. Tarallo[12], R. Taylor[12], R. Taylor[36], J. Thacker[15], K. A. Thorne[28], K. S. Thorne[5], A. Thüring[31], K. V. Tokmakov[19], C. Torres[29], C. Torrie[12], G. Traylor[15], M. Trias[32], W. Tyler[12], D. Ugolini[30], C. Ungarelli[34], H. Vahlbruch[31], M. Vallisneri[5], M. Varvella[12], S. Vass[12], A. Vecchio[34], J. Veitch[36], P. Veitch[33], S. Vigeland[7], A. Villar[12], C. Vorvick[14], S. P. Vyachanin[19], S. J. Waldman[12], L. Wallace[12], H. Ward[36], R. Ward[12], K. Watts[15], D. Webber[12], A. Weidner[2], A. Weinstein[12], R. Weiss[13], S. Wen[16], K. Wette[3], J. T. Whelan[18,1], D. M. Whitbeck[28], S. E. Whitcomb[12], B. F. Whiting[35], C. Wilkinson[14], P. A. Willems[12], B. Willke[31,2], I. Wilmut[23], W. Winkler[2], C. C. Wipf[13], S. Wise[35], A. G. Wiseman[42], G. Woan[36], D. Woods[42], R. Wooley[15], J. Worden[14], W. Wu[35], I. Yakushin[15], H. Yamamoto[12], Z. Yan[41], S. Yoshida[24], N. Yunes[28], M. Zanolin[13], L. Zhang[12], C. Zhao[41], N. Zotov[17], M. Zucker[15], H. zur Mühlen[31], J. Zweizig[12],

The LIGO Scientific Collaboration, http://www.ligo.org

[1]Albert-Einstein-Institut, Max-Planck-Institut für Gravitationsphysik, D-14476 Golm, Germany

[2]Albert-Einstein-Institut, Max-Planck-Institut für Gravitationsphysik, D-30167 Hannover, Germany

[3]Australian National University, Canberra, 0200, Australia

[4]California Institute of Technology, Pasadena, CA 91125, USA

[5]Caltech-CaRT, Pasadena, CA 91125, USA

[6]Cardiff University, Cardiff, CF2 3YB, United Kingdom

[7]Carleton College, Northfield, MN 55057, USA

[8]Columbia University, New York, NY 10027, USA

[9]Embry-Riddle Aeronautical University, Prescott, AZ 86301 USA

[10]Hobart and William Smith Colleges, Geneva, NY 14456, USA

[11]Inter-University Centre for Astronomy and Astrophysics, Pune - 411007, India

[12]LIGO - California Institute of Technology, Pasadena, CA 91125, USA

[13]LIGO - Massachusetts Institute of Technology, Cambridge, MA 02139, USA

[14]LIGO Hanford Observatory, Richland, WA 99352, USA

[15]LIGO Livingston Observatory, Livingston, LA 70754, USA

[16]Louisiana State University, Baton Rouge, LA 70803, USA

[17]Louisiana Tech University, Ruston, LA 71272, USA

[18]Loyola University, New Orleans, LA 70118, USA

[19]Moscow State University, Moscow, 119992, Russia

[20]NASA/Goddard Space Flight Center, Greenbelt, MD 20771, USA

[21]National Astronomical Observatory of Japan, Tokyo 181-8588, Japan

[22]Northwestern University, Evanston, IL 60208, USA

[23]Rutherford Appleton Laboratory, Chilton, Didcot, Oxon OX11 0QX United Kingdom

[24]Southeastern Louisiana University, Hammond, LA 70402, USA

[25]Southern University and A&M College, Baton Rouge, LA 70813, USA

[26]Stanford University, Stanford, CA 94305, USA

[27]Syracuse University, Syracuse, NY 13244, USA

[28]The Pennsylvania State University, University Park, PA 16802, USA

[29]The University of Texas at Brownsville and Texas Southmost College, Brownsville, TX 78520, USA

[30]Trinity University, San Antonio, TX 78212, USA

ABSTRACT

The Laser Interferometer Gravitational-wave Observatory (LIGO) has performed the fourth science run, S4, with significantly improved interferometer sensitivities with respect to previous runs. Using data acquired during this science run, we place a limit on the amplitude of a stochastic background of gravitational waves. For a frequency independent spectrum, the new limit is $\Omega_{\rm GW} < 6.5 \times 10^{-5}$. This is currently the most sensitive result in the frequency range 51-150 Hz, with a factor of 13 improvement over the previous LIGO result. We discuss complementarity of the new result with other constraints on a stochastic background of gravitational waves, and we investigate implications of the new result for different models of this background.

Subject headings: gravitational waves

1. Introduction

A stochastic background of gravitational waves (GWs) is expected to arise as a superposition of a large number of unresolved sources, from different directions in the sky, and

[31]Universität Hannover, D-30167 Hannover, Germany

[32]Universitat de les Illes Balears, E-07122 Palma de Mallorca, Spain

[33]University of Adelaide, Adelaide, SA 5005, Australia

[34]University of Birmingham, Birmingham, B15 2TT, United Kingdom

[35]University of Florida, Gainesville, FL 32611, USA

[36]University of Glasgow, Glasgow, G12 8QQ, United Kingdom

[37]University of Maryland, College Park, MD 20742 USA

[38]University of Michigan, Ann Arbor, MI 48109, USA

[39]University of Oregon, Eugene, OR 97403, USA

[40]University of Rochester, Rochester, NY 14627, USA

[41]University of Western Australia, Crawley, WA 6009, Australia

[42]University of Wisconsin-Milwaukee, Milwaukee, WI 53201, USA

[43]Washington State University, Pullman, WA 99164, USA

with different polarizations. It is usually described in terms of the GW spectrum:

$$\Omega_{\rm GW}(f) = \frac{f}{\rho_c}\,\frac{d\rho_{\rm GW}}{df}\,, \tag{1}$$

where $d\rho_{\rm GW}$ is the energy density of gravitational radiation contained in the frequency range f to $f + df$ (Allen & Romano 1999), ρ_c is the critical energy density of the Universe, and f is frequency (for an alternative and equivalent definition of $\Omega_{\rm GW}(f)$ see, for example, (Baskaran et al. 2006)). In this paper, we will focus on power-law GW spectra:

$$\Omega_{\rm GW}(f) = \Omega_\alpha \left(\frac{f}{100\ {\rm Hz}}\right)^\alpha. \tag{2}$$

Here, Ω_α is the amplitude corresponding to the spectral index α. In particular, Ω_0 denotes the amplitude of the frequency-independent GW spectrum.

Many possible sources of stochastic GW background have been proposed and several experiments have searched for it (see (Maggiore 2000; Allen 1996) for reviews). Some of the proposed theoretical models are cosmological in nature, such as the amplification of quantum vacuum fluctuations during inflation (Grishchuk 1975), (Grishchuk 1997), (Starobinsky 1979), pre-big-bang models (Gasperini & Veneziano 1993), (Gasperini & Veneziano 2003), (Buonanno et al. 1997 phase transitions (Kosowsky et al. 1992), (Apreda et al. 2002), and cosmic strings (Caldwell & Allen 1992) (Damour & Vilenkin 2000), (Damour & Vilenkin 2005). Others are astrophysical in nature, such as rotating neutron stars (Regimbau & de Freitas Pacheco 2001), supernovae (Coward et al. 2002) or low-mass X-ray binaries (Cooray 2004).

A number of experiments have been used to constrain the spectrum of GW background at different frequencies. Currently, the most stringent constraints arise from large-angle correlations in the cosmic microwave background (CMB) (Allen & Koranda 1994; Turner 1997), from the arrival times of millisecond pulsar signals (Jenet et al. 2006), from Doppler tracking of the Cassini spacecraft (Armstrong et al. 2003), and from resonant bar GW detectors, such as Explorer and Nautilus (Astone et al. 1999). An indirect bound can be placed on the total energy carried by gravitational waves at the time of the Big-Bang Nucleosynthesis (BBN) using the BBN model and observations (Kolb & Turner 1990; Maggiore 2000; Allen 1996). Similarly, (Smith et al. 2006a) used the CMB and matter spectra to constrain the total energy density of gravitational waves at the time of photon decoupling.

Ground-based interferometer networks can directly measure the GW strain spectrum in the frequency band 10 Hz - few kHz, by searching for correlated signal beneath uncorrelated detector noise. LIGO has built three power-recycled Michelson interferometers, with a Fabry-Perot cavity in each orthogonal arm. They are located at two sites, Hanford, WA, and Livingston Parish, LA. There are two collocated interferometers at the WA site: H1, with

4km long arms, and H2, with 2km arms. The LA site contains L1, a 4km interferometer, similar in design to H1. The detector configuration and performance during LIGO's first science run (S1) was described in (Abbott et al. 2004a). The data acquired during that run was used to place an upper limit of $\Omega_0 < 44.4$ on the amplitude of a frequency independent GW spectrum, in the frequency band 40-314 Hz (Abbott et al. 2004b). This limit, as well as the rest of this paper, assumes the present value of the Hubble parameter $H_0 = 72$ km/s/Mpc or, equivalently, $h_{100} = H_0/(100\ \mathrm{km/s/Mpc}) = 0.72$ (Bennet et al. 2003). The most recent bound on the amplitude of the frequency independent GW spectrum from LIGO is based on the science run S3: $\Omega_0 < 8.4 \times 10^{-4}$ for a frequency-independent spectrum in the 69-156 Hz band (Abbott et al. 2005).

In this paper, we report much improved limits on the stochastic GW background around 100 Hz, using the data acquired during the LIGO science run S4, which took place between February 22, 2005 and March 23, 2005. The sensitivity of the interferometers during S4, shown in Figure 1, was significantly better as compared to S3 (by a factor 10× at certain frequencies), which leads to an order of magnitude improvement in the upper limit on the amplitude of the stochastic GW background: $\Omega_0 < 6.5 \times 10^{-5}$ for a frequency-independent spectrum over the 51-150 Hz band.

This limit is beginning to probe some models of the stochastic GW background. As examples, we investigate the implications of this limit for cosmic strings models and for pre-big-bang models of the stochastic gravitational radiation. In both cases, the new LIGO result excludes parts of the parameter space of these models.

The organization of this paper is as follows. In Section 2 we review the analysis procedure and present the results in Section 3. In Section 4, we discuss some of the implications of our results for models of a stochastic GW background, as well as the complementarity between LIGO and other experimental constraints on a stochastic GW background. We conclude with future prospects in Section 5.

2. Analysis

2.1. Cross-Correlation Method

The cross-correlation method for searching for a stochastic GW background with pairs of ground-based interferometers is described in (Allen & Romano 1999). We define the following cross-correlation estimator:

$$Y = \int_0^{+\infty} df\, Y(f)$$

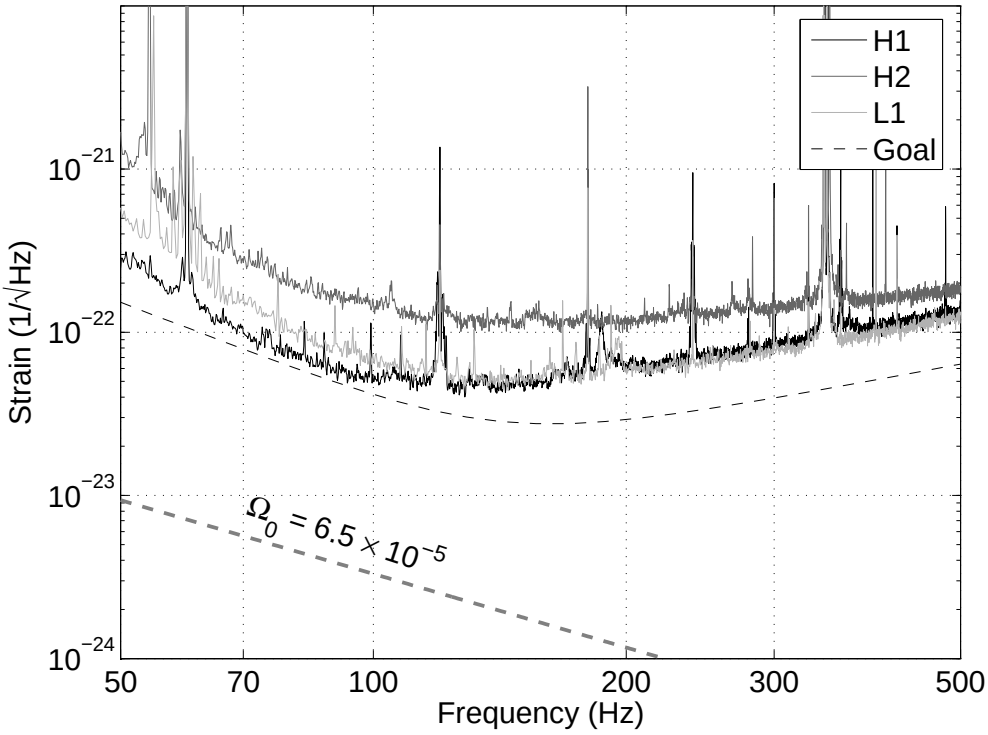

Fig. 1.— Typical strain amplitude spectra of LIGO interferometers during the science run S4 (solid curves top-to-bottom at 70 Hz: H2, L1, H1). The black dashed curve is the LIGO sensitivity goal. The gray dashed curve is the strain amplitude spectrum corresponding to the limit presented in this paper for the frequency-independent GW spectrum $\Omega_0 < 6.5 \times 10^{-5}$.

$$= \int_{-\infty}^{+\infty} df \int_{-\infty}^{+\infty} df' \, \delta_T(f - f') \, \tilde{s}_1(f)^* \, \tilde{s}_2(f') \, \tilde{Q}(f') \, , \tag{3}$$

where δ_T is a finite-time approximation to the Dirac delta function, $\tilde{s}_1$ and $\tilde{s}_2$ are the Fourier transforms of the strain time-series of two interferometers, and $\tilde{Q}$ is a filter function. Assuming that the detector noise is Gaussian, stationary, uncorrelated between the two interferometers, and much larger than the GW signal, the variance of the estimator Y is given by:

$$\begin{aligned} \sigma_Y^2 &= \int_0^{+\infty} df \; \sigma_Y^2(f) \\ &\approx \frac{T}{2} \int_0^{+\infty} df P_1(f) P_2(f) \mid \tilde{Q}(f) \mid^2 , \end{aligned} \tag{4}$$

where $P_i(f)$ are the one-sided power spectral densities (PSDs) of the two interferometers and T is the measurement time. Optimization of the signal-to-noise ratio leads to the following form of the optimal filter (Allen & Romano 1999):

$$\tilde{Q}(f) = \mathcal{N} \, \frac{\gamma(f) S_{\rm GW}(f)}{P_1(f) P_2(f)} \, , \tag{5}$$

where

$$S_{\rm GW}(f) = \frac{3H_0^2}{10\pi^2} \, \frac{\Omega_{\rm GW}(f)}{f^3} \, , \tag{6}$$

and $\gamma(f)$ is the overlap reduction function, arising from the different locations and orientations of the two interferometers. As shown in Figure 2, the identical antenna patterns of the collocated Hanford interferometers imply $\gamma(f) = 1$. For the Hanford-Livingston pair the overlap reduction is significant above 50 Hz. In Equations 5 and 6, $S_{\rm GW}(f)$ is the strain power spectrum of the stochastic GW background to be searched. Assuming a power-law template GW spectrum with index α (see Equation 2), the normalization constant $\mathcal{N}$ in Equation 5 is chosen such that $< Y >= \Omega_\alpha T$.

In order to deal with data non-stationarity, and for purposes of computational feasibility, the data for an interferometer pair are divided into many intervals of equal duration, and Y_I and σ_{Y_I} are calculated for each interval I. The data in each interval are decimated from 16384 Hz to 1024 Hz and high-pass filtered with a 40 Hz cut-off. They are also Hann-windowed to avoid spectral leakage from strong lines present in the data. Since Hann-windowing effectively reduces the interval length by 50%, the data intervals are overlapped by 50% to recover the original signal-to-noise ratio. The effects of windowing are taken into account as discussed in (Abbott et al. 2004b).

The PSDs for each interval (needed for the calculation of $Q_I(f)$ and of σ_{Y_I}) are calculated using the two neighboring intervals. This approach avoids a bias that would otherwise exist

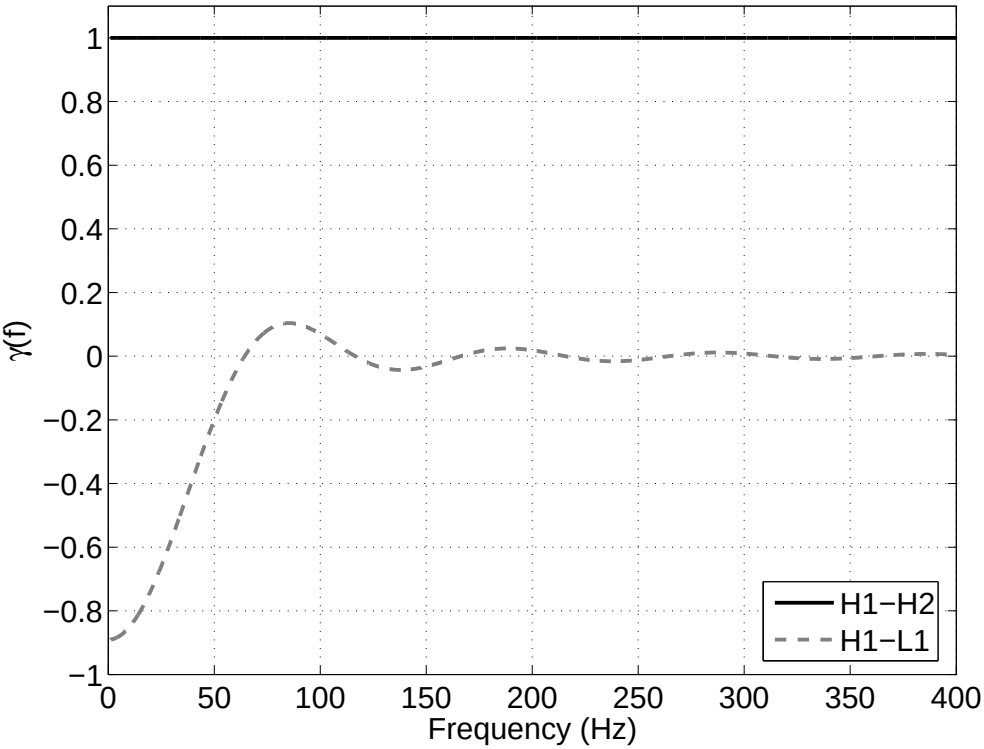

Fig. 2.— Overlap reduction function for the Hanford-Hanford pair (black solid) and for the Hanford-Livingston pair (gray dashed).

due to a non-zero covariance between the cross-power $Y(f)$ and the power spectra estimated from the same data (Bendat & Piersol 2000). It also allows for a stationarity cut, which we will describe in more detail below.

We consider two interval durations and frequency resolutions:

- 60-sec duration with 1/4 Hz resolution: the PSDs are calculated by averaging 58 50% overlapping periodograms (based on the two neighboring 60-sec intervals) in Welch's modified periodogram method.
- 192-sec duration with 1/32 Hz resolution: the PSDs are calculated by averaging 22 50% overlapping periodograms (based on the two neighboring 192-sec intervals) in Welch's modified periodogram method.

As we will discuss below, the 60-sec intervals allow better sensitivity to noise transients and are better suited for data-stationarity cuts, while the 192-sec intervals allow higher frequency resolution of the power and cross-power spectra and are better suited for removing sharp lines from the analysis.

The data for a given interval I are Fourier transformed and rebinned to the frequency resolution of the optimal filter to complete the calculation of Y_I (Eq. 3). Both the PSDs and the Fourier transforms of the data are calibrated using interferometer response functions, determined for every minute of data using a measurement of the interferometer response to a sinusoidal calibration force. To maximize the signal-to-noise ratio, the intervals are combined by performing a weighted average (with weights $1/\sigma^2_{Y_I}$), properly accounting for the 50% overlapping as discussed in (Lazzarini & Romano 2004).

2.2. Identification of Correlated Instrumental Lines

The results of this paper are based on the Hanford-Livingston interferometer pairs, for which the broadband instrumental correlations are minimized. Nevertheless, it is still necessary to investigate if there are any remaining periodic instrumental correlations. We do this by calculating the coherence over the whole S4 run. The coherence is defined as:

$$\Gamma(f) = \frac{|s_1^*(f)s_2(f)|^2}{P_1(f)P_2(f)}. \tag{7}$$

The numerator is the square of the cross-spectral density (CSD) between the two interferometers, and the denominator contains the two power spectral densities (PSDs). We average

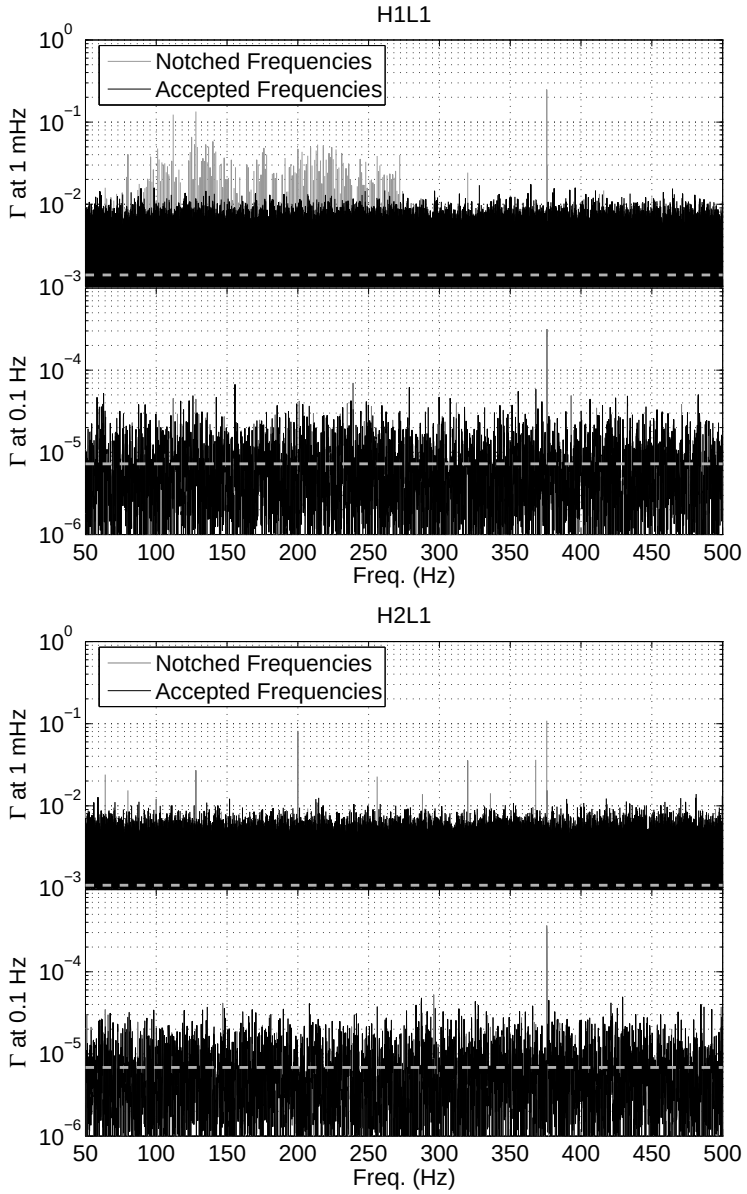

Fig. 3.— Coherence calculated for the H1L1 pair (top) and for the H2L1 pair (bottom) over all of S4 data for 1 mHz resolution and 100 mHz resolution. The horizontal dashed lines indicate $1/N_{avg}$ - the expected level of coherence after averaging over N_{avg} time-periods with uncorrelated spectra. The line at 376 Hz is one of the simulated pulsar lines.

the CSD and the PSDs over the whole run at two different resolutions: 1 mHz and 100 mHz. Figure 3 shows the results of this calculation for the H1L1 pair and for the H2L1 pair.

At 1 mHz resolution, a forest of sharp 1 Hz harmonic lines can be observed. These lines were likely caused by the sharp ramp of a one-pulse-per-second signal, injected into the data acquisition system to synchronize it with the Global Positioning System (GPS) time reference. After the S4 run ended, the sharp ramp signal was replaced by smooth sinusoidal signals, with the goal of significantly reducing the 1 Hz harmonic lines in future LIGO data runs. In addition to the 1 Hz lines, the 1 mHz coherence plots in Figure 3 also include some of the simulated pulsar lines, which were injected into the differential-arm servo of the interferometers by physically moving the mirrors. Both the 1 Hz harmonics and the simulated pulsar lines can be removed in the final analysis, and we will discuss this further in Section 3. Figure 4 shows that the histogram of the coherence at 1 mHz resolution follows the expected exponential distribution, if one ignores the 1 Hz harmonics and the simulated pulsar lines.

2.3. Data Quality Cuts

In our analysis, we include time periods during which both interferometers are in low-noise, science mode. We exclude:

- Time-periods when digitizer signals saturate.
- 30-sec intervals prior to each lock loss. These intervals are known to be particularly noisy.

We then proceed to calculate Y_I and σ_{Y_I} for each interval I, and define three data-quality cuts. First, we reject intervals known to contain large glitches in one interferometer. These intervals were identified by searching for discontinuities in the PSD trends over the whole S4 run. Second, we reject intervals for which σ_{Y_I} is anomalously large. In particular, for the 192-sec analysis, we require $\sigma_{Y_I} < 1$ sec for the H1L1 pair, and $\sigma_{Y_I} < 2$ sec for the H2L1 pair (recall that Y is normalized such that $< Y >= \Omega_\alpha T$, with $T = 192$ sec in this case). The glitch cut and the large-sigma cut largely overlap, and are designed to remove particularly noisy time-periods from the analysis. Note, also, that due to the weighting with $1/\sigma_{Y_I}^2$, the contribution of these intervals to the final result would be suppressed, but we reject them from the analysis nevertheless. Third, we reject the intervals for which $\Delta\sigma = |\sigma_{Y_I} - \sigma'_{Y_I}|/\sigma_{Y_I} > \zeta$. Here, σ_{Y_I} is calculated using the two intervals neighboring interval I, and σ'_{Y_I} is calculated using the interval I itself. The optimization of threshold ζ is discussed below. The goal of

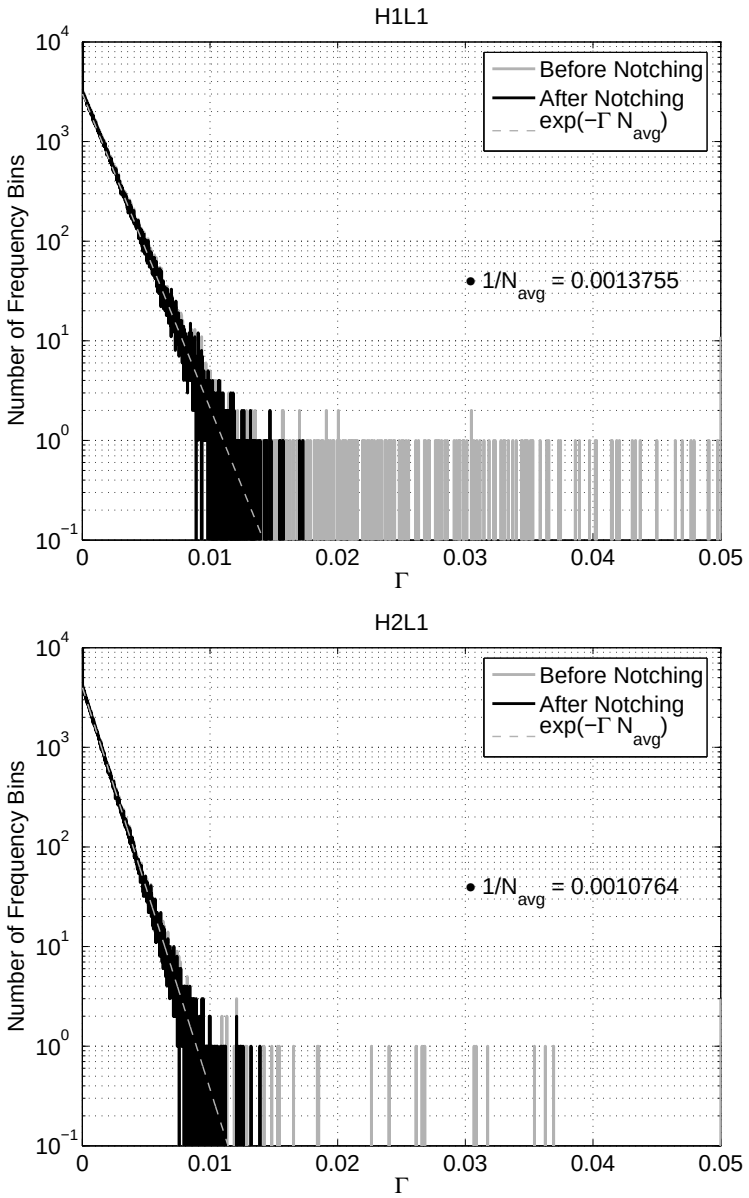

Fig. 4.— Histogram of the coherence for H1L1 (top) and H2L1 (bottom) at 1 mHz resolution follows the expected exponential distribution, with exponent coefficient N_{avg} (the number of time-periods over which the average is made).

this cut is to capture noise-transients in the data, and reject them from the analysis. Figure 5 shows the impact of these cuts for the H1L1 pair, analyzed with 192-sec segments, 1/32 Hz resolution, and with $\zeta = 0.3$. This Figure also shows daily variation in the sensitivity to stochastic GW background, arising from the variation in the strain sensitivity of the interferometers, which is typically worse during the week-days than during the weekends or nights.

Figure 6 shows the distribution of the residuals for the same analysis. For a given interval I, the residual is defined as

$$\frac{Y_I - < Y >}{\sigma_{Y_I}}. \tag{8}$$

Note that the data quality cuts remove outliers from the residual distribution, hence making the data more stationary. After the cuts, the Kolmogorov-Smirnov test indicates that the residual distribution is consistent with a Gaussian, for both H1L1 and H2L1 analyses with 192-sec intervals, 1/32 Hz resolution, and $\zeta = 0.3$.

3. Results

3.1. New Upper Limit

We performed a "blind" analysis for the H1L1 and the H2L1 pairs with 60-sec intervals, 1/4 Hz resolution, and $\zeta = 0.2$. To avoid biasing the results, all data-quality cuts were defined based on studies done with a 0.1 sec time-shift between the two interferometers in a pair. Such a time-shift removes any GW correlations, without significantly affecting the instrumental noise performance. After the data quality cuts were finalized, we made one last pass through the data, with zero time-shift, and obtained the final results of the blind analysis.

The results from the blind analysis for the frequency-independent template spectrum ($\alpha = 0$) are listed in the first row of Table 1 for H1L1 and in the first row of Table 2 for H2L1. These results show no evidence of a stochastic GW background. After completing the blind analysis, we discovered that the instrumental 1 Hz harmonic lines, discussed in Section 2.2, are correlated between the two sites. We felt compelled on scientific grounds not to ignore these correlations, even though they had been discovered after our initial, blind, analysis was complete.

In order to remove from our results any possible influence of the correlated lines, we repeated our analysis with refined frequency resolution of 1/32 Hz. We increased the interval

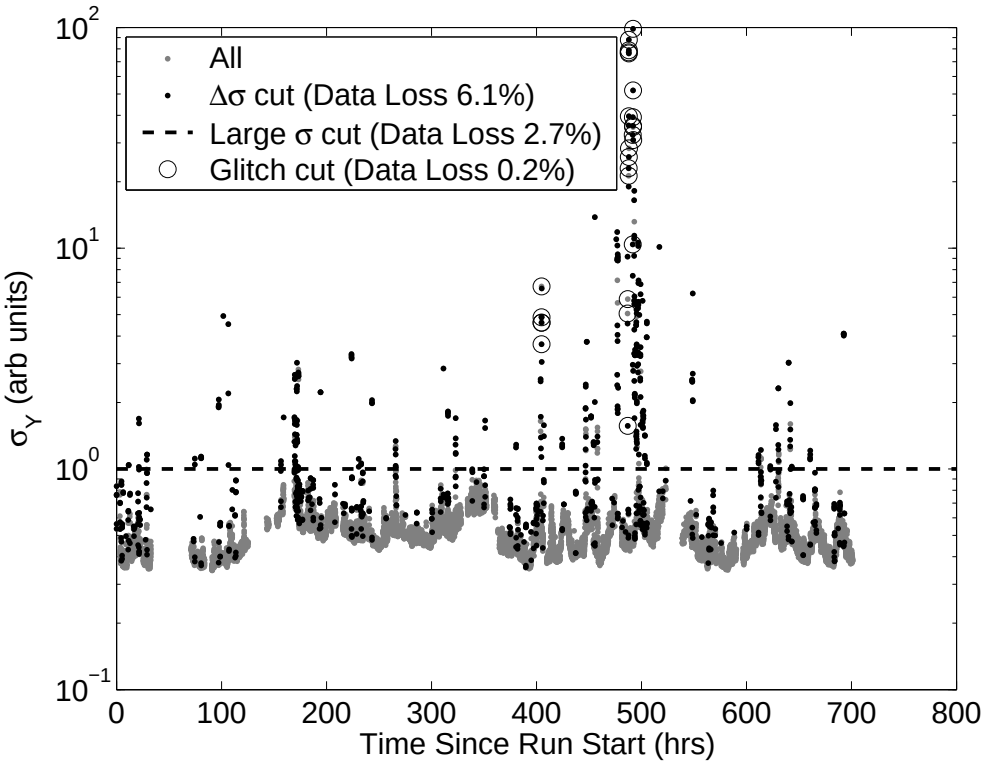

Fig. 5.— Trend of σ_{Y_I} over the whole S4 run for the 192-sec intervals of H1L1 pair. The dashed line denotes the large σ cut: segments lying above this line are removed from analysis. Note the daily variation in the sensitivity of this pair.

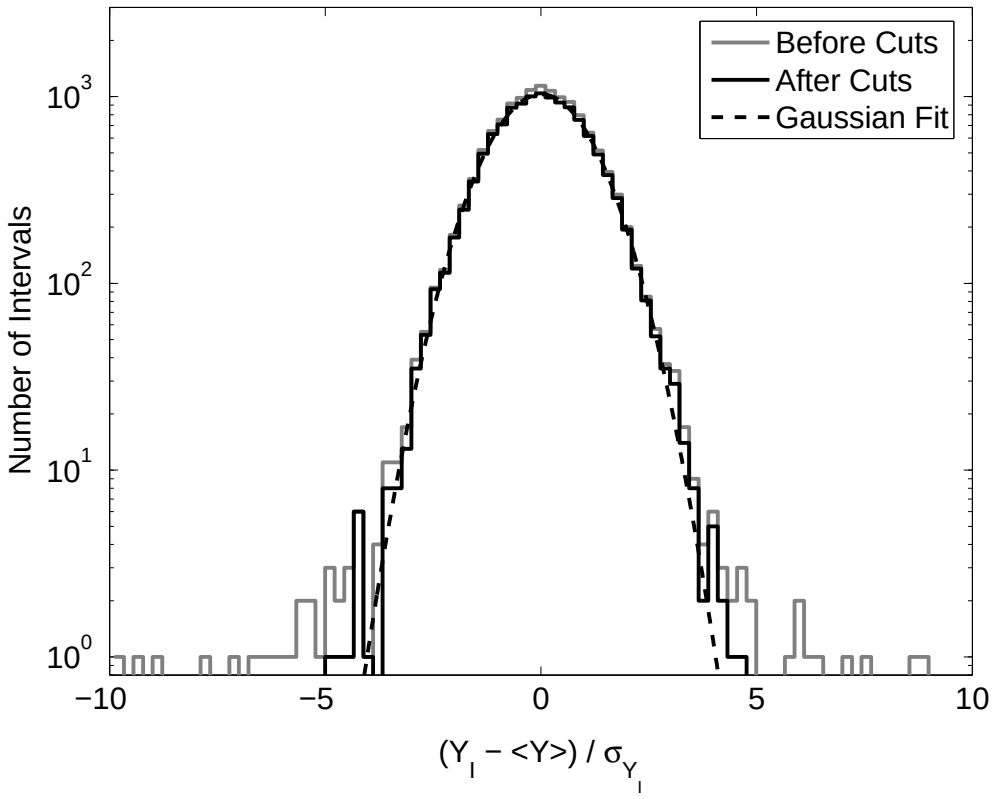

Fig. 6.— Distribution of residuals for the H1L1 pair with 192-sec segments: all data are shown in gray, data that passes data quality cuts are shown in black, and the Gaussian fit to the black histogram is shown as a dashed curve.

length from 60-sec to 192-sec, which implies that the PSDs are estimated by averaging 22 50% overlapping periodograms. These changes allowed us to exclude the 1 Hz harmonics from the analysis while losing only $\sim 3\%$ of the bandwidth. The drawback, however, was that the 192-sec analysis was less able to identify and exclude the noise-transients than the 60-sec analysis, as shown in Figure 7. As a result, the $\Delta\sigma$ cut was retuned for the 192-sec analysis after the 60-sec analysis with zero time-shift was completed.

We examined several methods of defining the data quality cuts for the 192-sec analysis. First, we calculated the $\Delta\sigma$ cut in the 60-sec analysis with $\zeta = 0.2$ (along with large sigma and glitch cuts), and then declared 192-sec intervals "bad" if they overlapped with the "bad" 60-sec intervals. This approach has the advantage that the 60-sec analysis is more sensitive to transients, and the disadvantage that a significant fraction of the data is rejected. The results of this approach are summarized in the second row of Tables 1 and 2. Second, we defined all cuts directly on 192-sec intervals. We varied the value of ζ (0.2, 0.3, and 0.4) and selected $\zeta = 0.3$ as the optimal parameter choice. This choice represents the best compromise between data loss and data quality: it rejects the least amount of data, while still excluding all residual outliers and preserving the Gaussianity of the data. The last three rows of Tables 1 and 2 summarize the results for the three values of ζ.

The 192-sec analysis was not performed blindly. However, it agrees with our blind 60-sec analysis very well, because the contribution of the correlated 1 Hz harmonic lines is only about 1.5σ. It is also more conservative than the blind analysis since the value of the theoretical error is larger due to a smaller amount of data available in the form of acceptable 192-sec intervals (as compared to the 60-sec intervals). It also properly handles the known instrumental correlations at 1 Hz harmonics. Hence, in the remaining part of the paper we will focus on the 192-sec analysis with $\zeta = 0.3$.

Figures 8 and 9 show the results of the 192-sec analysis with $\zeta = 0.3$ for H1L1 and H2L1 respectively. The top plots in these two Figures show the cummulative estimates for the frequency-independent GW template ($\alpha = 0$) as a function of time. They indicate that there is no particular time during the run that dominates the result. Moreover, the $\pm 1.65\sigma$ bounds converge as $\sim 1/\sqrt{T}$, as expected. The middle plots of the two Figures show the cross-correlation spectra (i.e. the integrand of Equation 3). They indicate that there is no particular frequency that dominates the result.

We perform a weighted average of the H1L1 and H2L1 results at each frequency bin (with inverse variances as weights). The resulting cross-correlation spectrum and the theoretical error are shown in Figure 10. The frequency range 51-150 Hz contributes 99% of the full sensitivity, as determined by the inverse combined variance. Integrating over this frequency range, we obtain the final estimate for the frequency-independent spectrum: $\Omega_0 = (-0.8 \pm$

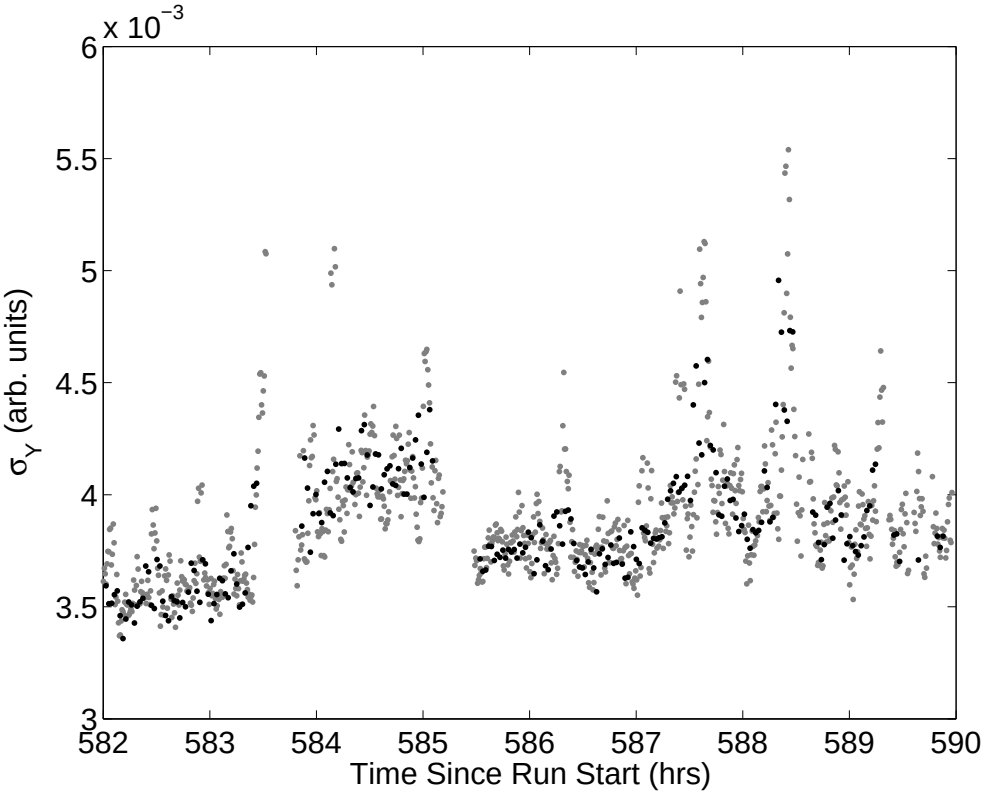

Fig. 7.— Trend of σ_Y for the 60-sec analysis (gray) and 192-sec analysis (black) over a short period of time. The two bands were scaled to overlap. Note that the gray band is wider, indicating that the 60-sec analysis is more sensitive to noise variations.

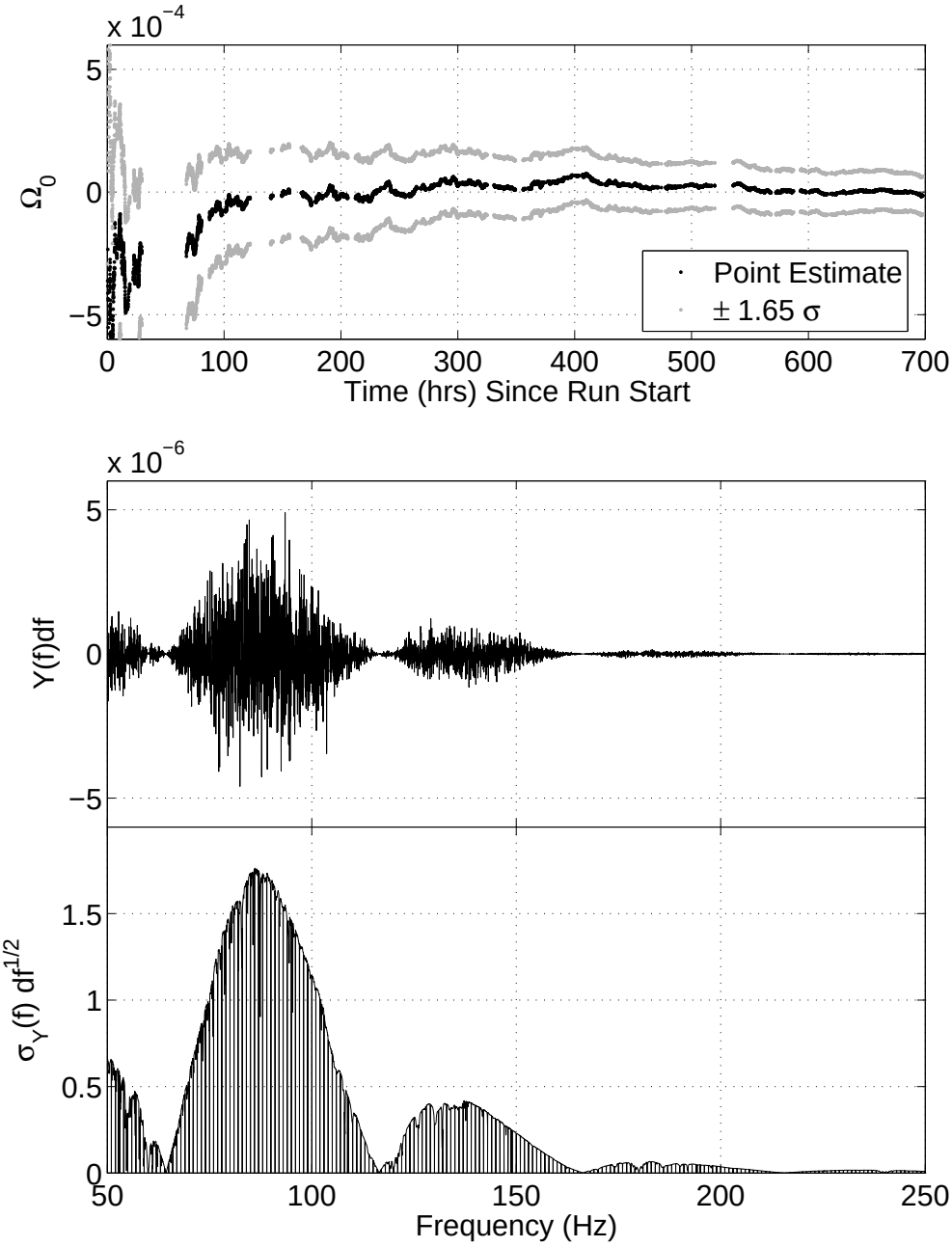

Fig. 8.— H1L1, 192-sec analysis with $\zeta = 0.3$. Top: Cummulative estimate of Ω_0 is shown as a function of time. Middle: cross-correlation spectrum $Y(f)$. Bottom: theoretical uncertainty $\sigma_Y(f)$ as a function of frequency.

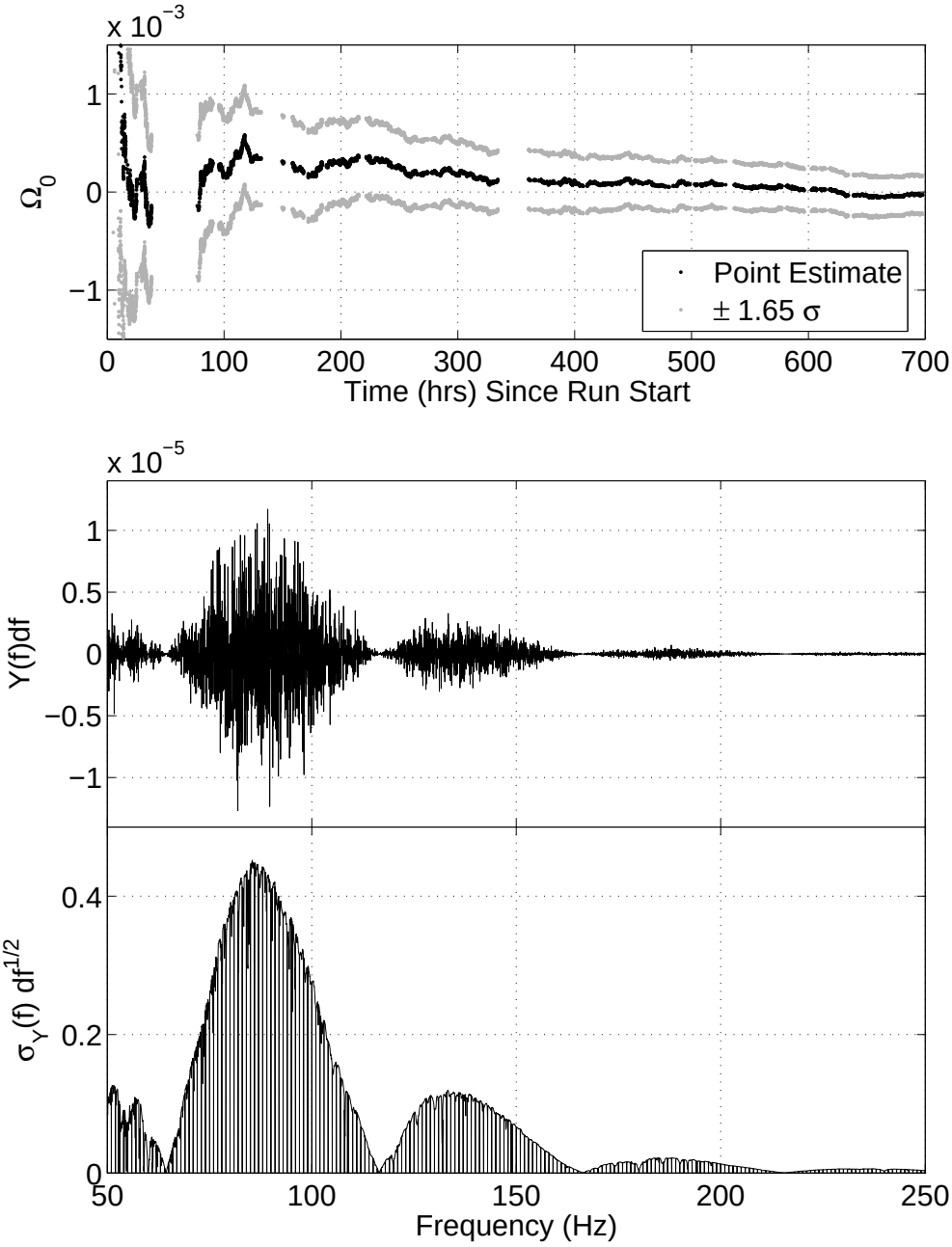

Fig. 9.— H2L1, 192-sec analysis with $\zeta = 0.3$. Top: Cummulative estimate of Ω_0 is shown as a function of time. Middle: cross-correlation spectrum $Y(f)$. Bottom: theoretical uncertainty $\sigma_Y(f)$ as a function of frequency.

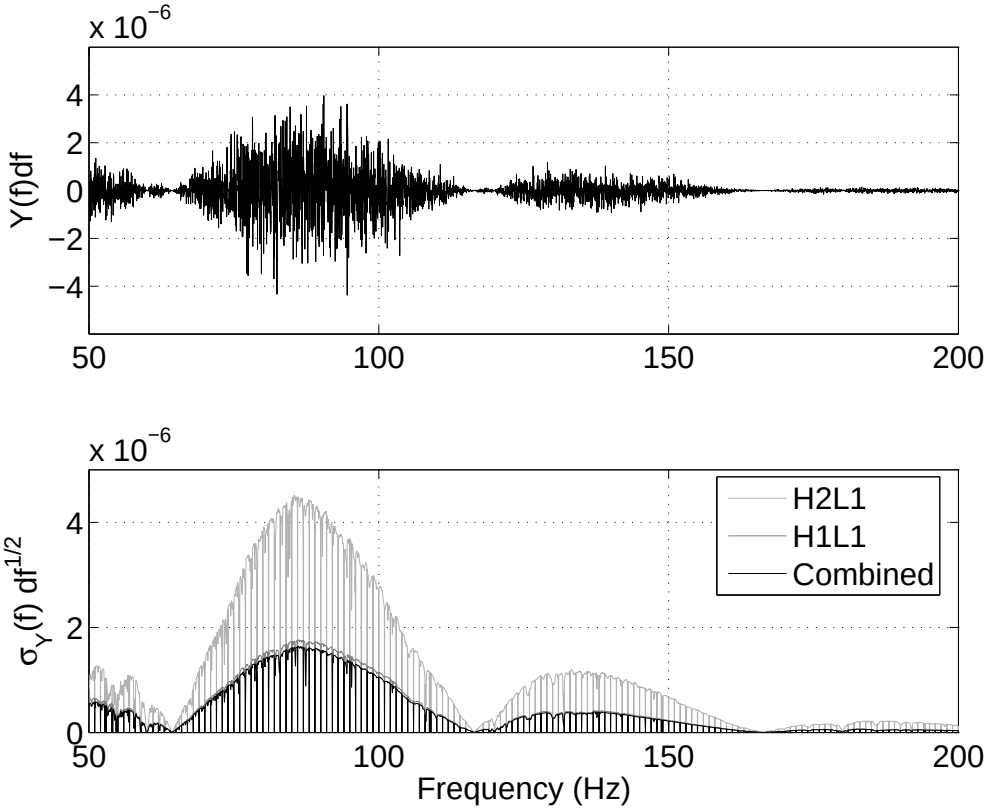

Fig. 10.— Combined H1L1 + H2L1 result, 192-sec analysis with $\zeta = 0.3$. Top: Combined cross-correlation spectrum. Bottom: Theoretical uncertainty $\sigma_Y(f)$.

Analysis	ζ	Fraction of Data Excluded	$\Omega_0(\times 10^{-5})$ before notching 50-500 Hz	$\Omega_0(\times 10^{-5})$ after notching 51-150 Hz	90% UL $(\times 10^{-5})$
60-sec (blind)	0.2	7.1%	6.4 ± 4.3	-	13.0
192-sec	conversion	21.0%	3.4 ± 4.9	-2.4 ± 5.0	7.0
192-sec	0.2	10.9%	6.1 ± 4.7	0.1 ± 4.8	8.0
192-sec	0.3	6.5%	4.8 ± 4.6	-0.7 ± 4.7	7.3
192-sec	0.4	5.0%	4.8 ± 4.6	-0.7 ± 4.7	7.3

Table 1: H1L1 results, for $h_{100} = 0.72$ and for a frequency-independent template spectrum ($\alpha = 0$). The first two columns define the analysis (interval duration and $\Delta\sigma$ cut). For the 192-sec analysis with ζ denoted as "conversion" (second row), the $\Delta\sigma$ cut was defined using the 60-sec analysis listed in the first row: the 192-sec segments are declared "bad" if they overlap with a "bad" 60-sec segment. The third column shows the fraction of the data lost to data-quality cuts. The fourth column lists the estimates of Ω_0 for the 50-500 Hz range before notching the 1 Hz harmonics and the simulated pulsar lines. The fifth column lists the estimates of Ω_0 for the $51 - 150$ Hz range after notching the 1 Hz harmonics and the simulated pulsar lines - this frequency range was determined to be optimal for the combined H1L1+H2L1 analysis (see text). The sixth column gives the 90% upper limit based on the result in the fifth column. For all analyses presented here, the distribution of the residual outliers was consistent with a Gaussian distribution (c.f. Figure 6; the Kolmogorov-Smirnov test statistic for comparing the two distributions was greater than 85% in all cases).

Analysis	ζ	Fraction of Data Excluded	$\Omega_0(\times 10^{-5})$ before notching 50-500 Hz	$\Omega_0(\times 10^{-5})$ after notching 51-150 Hz	90% UL $(\times 10^{-5})$
60-sec (blind)	0.2	4.1%	-8.2 ± 10.6	-	13.0
192-sec	conversion	10.7%	-3.9 ± 11.9	-7.2 ± 12.1	16.1
192-sec	0.2	6.1%	-1.7 ± 11.6	-4.2 ± 11.8	17.1
192-sec	0.3	4.6%	-0.6 ± 11.5	-3.3 ± 11.7	17.5
192-sec	0.4	3.8%	-3.1 ± 11.5	-6.1 ± 11.7	15.9

Table 2: H2L1 results, for $h_{100} = 0.72$ and for a frequency-independent template spectrum ($\alpha = 0$). The columns are as in Table 1. For all analyses presented here, the distribution of the residual outliers was consistent with a Gaussian distribution (the Kolmogorov-Smirnov test statistic for comparing the two distributions was greater than 52% in all cases).

4.3) $\times 10^{-5}$.

The dominant systematic uncertainty of this result comes from the amplitude calibration uncertainty of the interferometers. This uncertainty is estimated to be 5% (L1) and 8% (H1 and H2), and it is frequency-independent. The uncertainty in the phase of the interferometer strain response is negligible compared to the magnitude and statistical uncertainties. Similarly, the effect of timing errors, measured to be $\lesssim 4\ \mu$s, is negligible. Using hardware injections, we estimate that the effect of the timing errors on our point estimate is $\lesssim 0.2\%$.

We then construct the Bayesian posterior distribution for Ω_0 using the above estimate, following (Loredo 1990). We assume a Gaussian distribution for the amplitude calibration uncertainty (with mean 1 and standard deviation $\sqrt{0.05^2 + 0.08^2} = 0.093$), and we marginalize over it. We assume the prior distribution for Ω_0 to be the posterior distribution obtained in our previous analysis of the S3 data (Abbott et al. 2005). The 90% upper limit is the value of Ω_0 for which 90% of the posterior distribution lies between 0 and the upper limit. This procedure yields the Bayesian 90% UL on Ω_0 of 6.5×10^{-5}. This is an improvement by a factor 13× over the previous result in the same frequency band, established based on the science run S3 (Abbott et al. 2005). To investigate robustness of our result under different priors, we repeated the calculation using flat priors for the amplitude calibration uncertainties, and using a flat prior for Ω_0 between 0 and 8.4×10^{-4} (previous 90% UL by LIGO, (Abbott et al. 2005)). We found that these different choices of priors have less than 3% effect on the 90% upper limit.

Once the estimate is made for the frequency-independent spectrum, one can perform appropriate frequency-dependent scalings of $Y(f)$ and $\sigma_Y(f)$, recalculate the posterior distributions, and re-marginalize to obtain upper limits for other templates, such as the power-law templates with different spectral indices α (see Equation 2). Figure 11 shows the 90% UL as a function of the spectral index α obtained for this analysis. Similar results for the S3 run of LIGO, as well as the expected sensitivities of H1L1 and H1H2 pairs assuming 1 year of exposure and design interferometer sensitivities, are also shown. The frequency range of interest is defined to include 99% of the full sensitivity, as determined by the inverse variance. For the S4 result, the frequency range varies between $(50 - 107)$ Hz for $\alpha = -3$ and $(73 - 288)$ Hz for $\alpha = +3$, as shown in the bottom plot of Figure 11. Note that the expected sensitivity of the collocated Hanford interferometer pair (H1H2) is significantly better than that of the H1L1 pair due to the better antenna pattern overlap (see Figure 2). However, this pair is also more susceptible to instumentally correlated noise. New analysis methods are being pursued to estimate and suppress these instrumental correlations (Fotopoulos 2006).

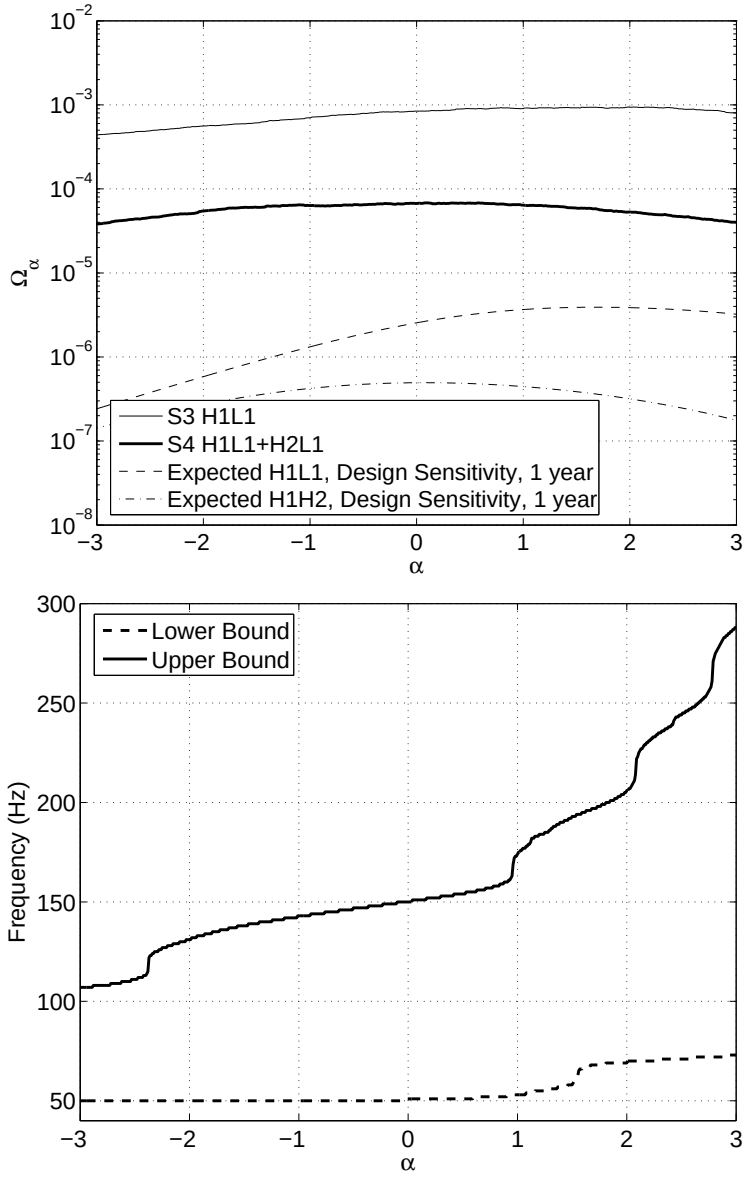

Fig. 11.— Top: 90% UL on Ω_α as a function of α for S3 H1L1 and S4 H1L1+H2L1 combined, and expected final sensitivities of LIGO H1L1 and H1H2 pairs, assuming LIGO design sensitivity and one year of exposure. Bottom: Frequency band containing 99% of the full sensitivity (as determined by the inverse variance) is plotted as a function of α for the S4 result.

3.2. Signal Injections

We exercise the analysis procedure described above using simulated stochastic signals injected into the data both in software and in hardware - see (Bose et al. 2003). In particular, we verify that the recovery of the injected signals is not affected by the data-quality cuts we impose. The hardware injections are performed by physically moving the mirrors to simulate a stochastic GW signal. Three hardware injections were performed during the S4 run, all using a frequency-independent GW spectrum ($\alpha = 0$). Table 3 summarizes the recovery of all of the hardware injections. Figure 12 shows the cross-correlation spectrum for injection 3. It also shows the inverse Fourier transform of the spectrum, which is equivalent to the estimate of Ω_0 for different values of time-lag between two interferometers (for short time-lags).

Injection	H1L1 Expected ($\times 10^{-2}$)	H1L1 Recovered ($\times 10^{-2}$)	H2L1 Expected ($\times 10^{-2}$)	H2L1 Recovered ($\times 10^{-2}$)
1	9.1	$7.9 \pm 0.2 \pm 0.8$	7.9	$6.9 \pm 0.4 \pm 0.6$
2	2.5	$2.5 \pm 0.4 \pm 0.2$	2.3	$1.5 \pm 0.6 \pm 0.2$
3	1.1	$0.95 \pm 0.04 \pm 0.10$	-	-

Table 3: Summary of the hardware injection amplitudes during S4. The second and fourth columns indicate the expected injection amplitudes for H1L1 and H2L1 respectively, based on the signal injected into the differential-arm servo. The third and the fifth columns list the recovered values using the H1L1 and H2L1 pairs respectively. The recovered values are listed with statistical errors (as defined in Equation 4), and with systematic errors (estimated using 5% calibration uncertainty in L1 and 8% calibration uncertainty in H1 and H2, added in quadrature). For injection 3, the data of H2 interferometer were compromised due to a failure of the interferometer's laser.

We performed a sequence of software injections, where the injected signal is simply added to the interferometer data in the analysis. We performed 10 trials for 4 injection amplitudes using about 1/3 of the S4 H1L1 data. Figure 13 shows that the signal is successfully recovered down to 1×10^{-4} in Ω_0. Moreover, the theoretical error bars agree well with the standard deviation over the 10 trials. All injections were performed assuming a frequency-independent GW spectrum ($\alpha = 0$).

4. Implications

In this Section, we investigate the implications of the new upper limit for some of the models of the stochastic GW background. We also discuss the complementarity of our result with various other experimental constraints on the stochastic GW background.

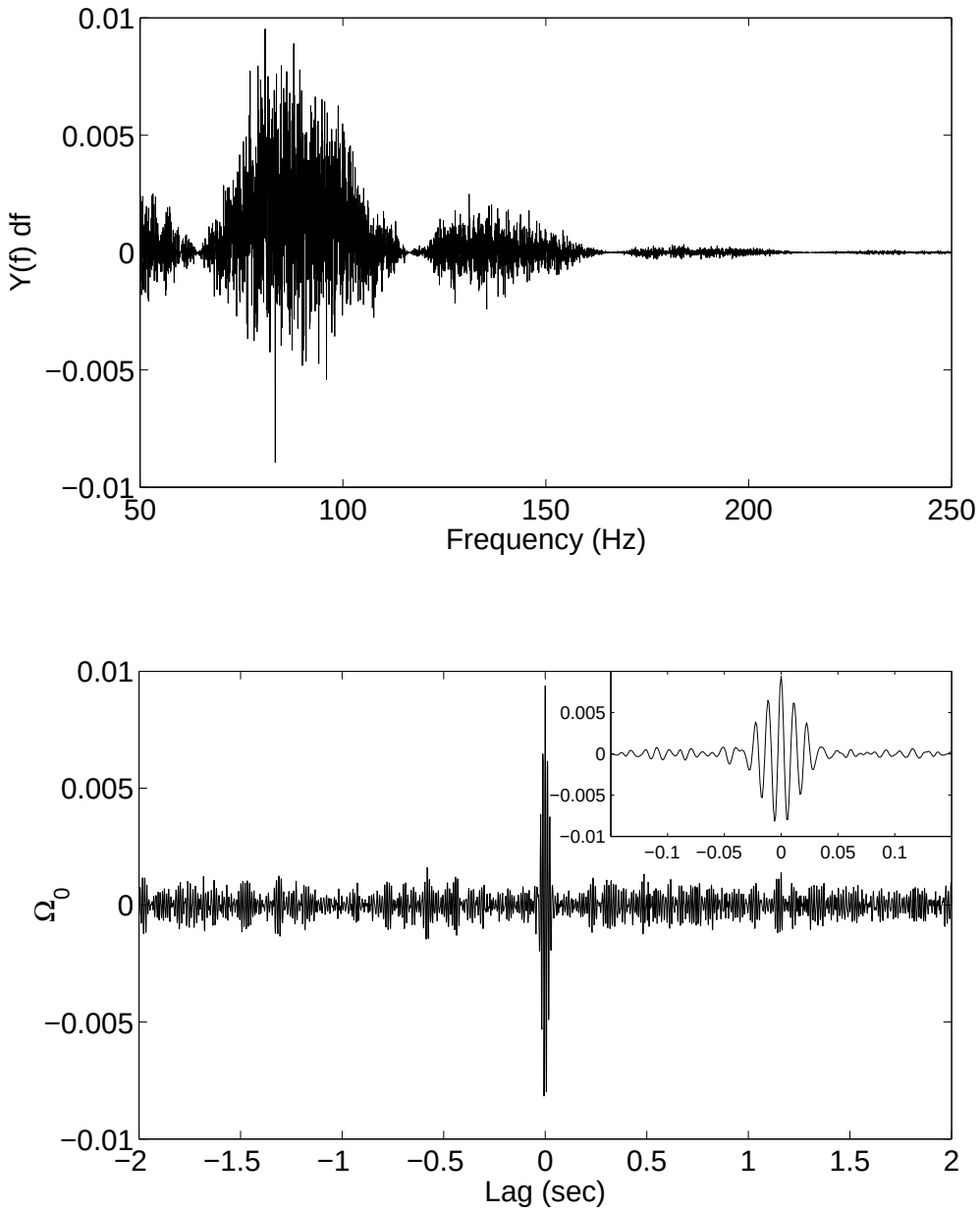

Fig. 12.— H1L1 injection 3 (with intended injection amplitude $\Omega_0 = 1.1 \times 10^{-2}$). Top: Cross-correlation spectrum $Y(f)$. Bottom: Inverse Fourier transform of the cross-correlation spectrum indicates the clear signal at zero lag. The inset plot is a zoom-in around zero lag.

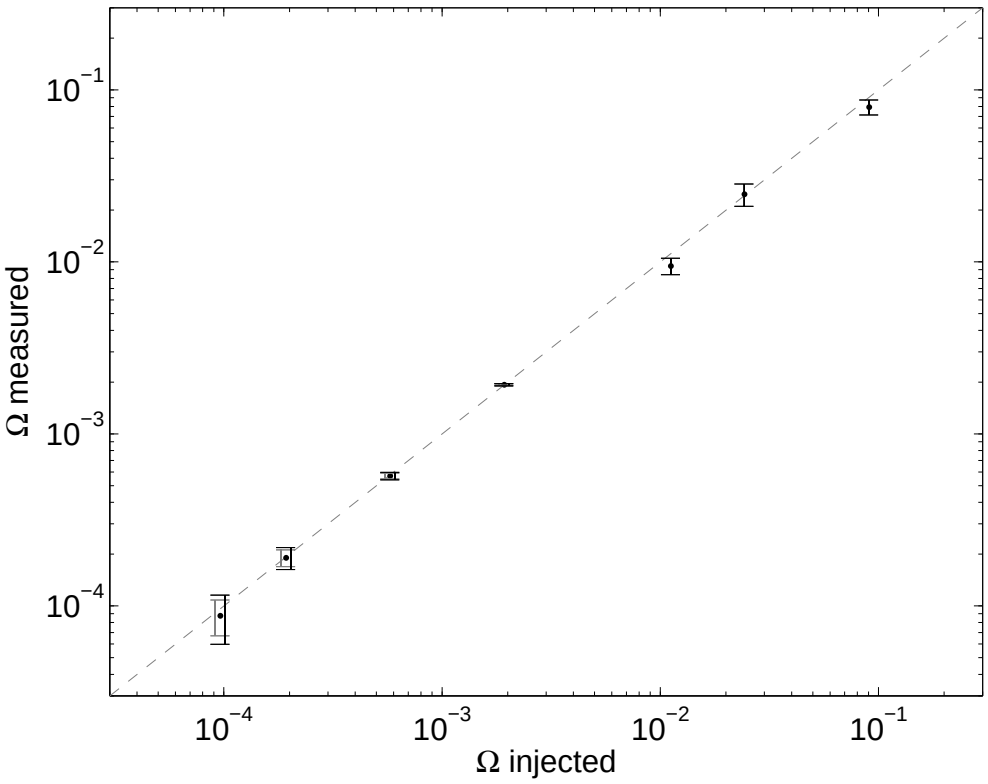

Fig. 13.— Injections using H1L1 data: 10 trials were performed for software injections with amplitudes $\Omega_0 = 1 \times 10^{-4}$, 2×10^{-4}, 6×10^{-4}, and 2×10^{-3}. The left(gray) error bars denote the theoretical errors, while the right(black) error bars denote the standard errors over the 10 trials. The remaining points correspond to the three hardware injections listed in Table 3; their error bars correspond to statistical and systematic errors added in quadrature, as shown in Table 3.

4.1. Complementarity with Other Measurements and Observations

Figure 14 compares different experiments and some of the theoretical models. For wavelengths larger than the horizon size at the surface of last scattering (redshifted to today, this corresponds to frequencies below $\sim 10^{-16}$ Hz), the COBE observations of the CMB place an upper limit on the stochastic gravitational wave background of $\Omega_{\rm GW}(f) < 1.3 \times 10^{-13}$ (Allen & Koranda 1994). In standard inflationary models (Turner 1997), the GW spectrum is expected to be (almost) flat at frequencies above $\sim 10^{-16}$ Hz.

The fluctuations in the arrival times of millisecond pulsar signals can be used to place a bound at $\sim 10^{-8}$ Hz (Jenet et al. 2006): $\Omega_{\rm GW}(f) < 3.9 \times 10^{-8}$ (assuming frequency independent GW spectrum). Similarly, Doppler tracking of the Cassini spacecraft can be used to arrive at yet another bound, in the $10^{-6} - 10^{-3}$ Hz band (Armstrong et al. 2003): $\Omega_{\rm GW}(f) < 0.027$.

If the energy density carried by the gravitational waves at the time of Big-Bang Nucleosynthesis (BBN) were large, the amounts of the light nuclei produced in the process could be altered. Hence, the BBN model and observations can be used to constrain the total energy carried by gravitational waves at the time of nucleosynthesis (Kolb & Turner 1990; Maggiore 2000; Allen 1996):

$$\int \Omega_{\rm GW}(f)\, d(\ln f) < 1.1 \times 10^{-5}\ (N_\nu - 3), \tag{9}$$

where N_ν is the effective number of relativistic species at the time of BBN. Measurements of the light-element abundances, combined with the WMAP data, give the following 95% upper bound: $N_\nu - 3 < 1.4$ (Cyburt et al. 2005). This limit translates into $\int \Omega_{\rm GW}(f)\, d(\ln f) < 1.5 \times 10^{-5}$. This bound applies down to $\sim 10^{-10}$ Hz, corresponding to the horizon size at the time of BBN.

Gravitational waves are also expected to leave a possible imprint on the CMB and matter spectra, similar to that of massless neutrinos. (Smith et al. 2006a) used recent measurements of the CMB anisotropy spectrum, galaxy power spectrum, and of the Lyman$-\alpha$ forest, to constrain the energy density carried by gravitational waves to $\int \Omega_{\rm GW}(f)\, d(\ln f) < 1.3 \times 10^{-5}$ for homogeneous initial conditions. This bound is competitive with the BBN bound and it extends down to $\sim 10^{-15}$ Hz, corresponding to the horizon size at the time of CMB decoupling. It is also expected to improve as new experiments come online (such as Planck or CMBPol).

The LIGO results apply to the frequency region around 100 Hz. The result discussed in this paper is an improvement by a factor 13× over the previous LIGO result in the 100 Hz region, for a frequency-independent spectrum of GW background. A one-year run at design

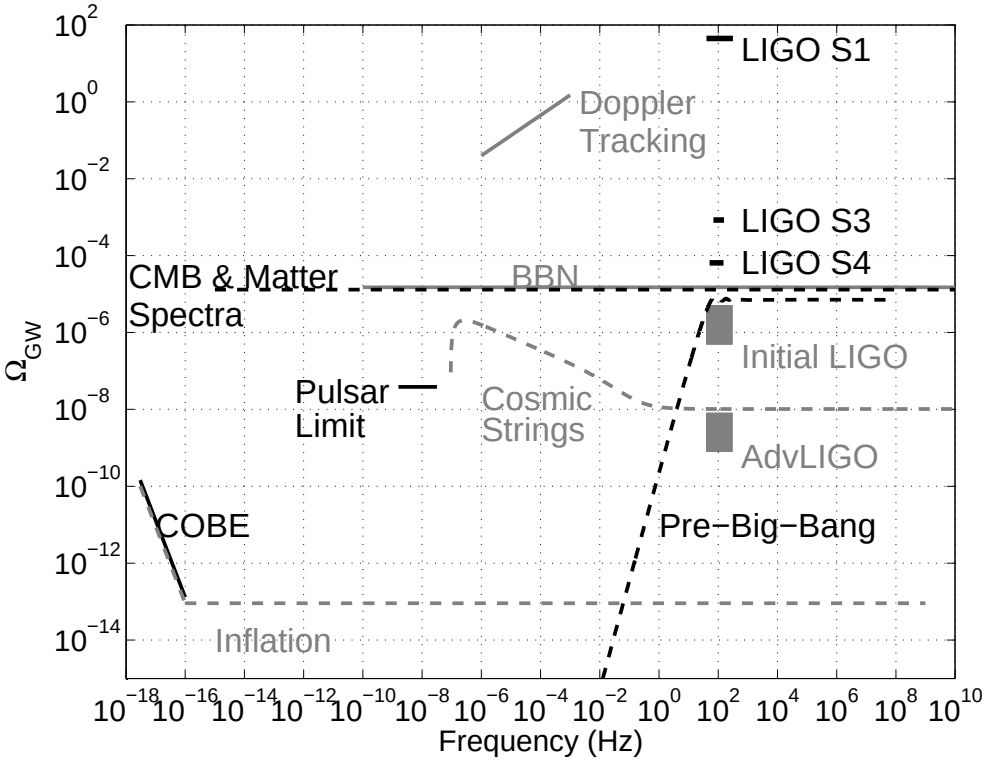

Fig. 14.— Landscape plot (see text for details). The curves corresponding to inflationary, cosmic-string, and pre-big-bang models are examples; significant variations of the predicted spectra are possible as the model parameters are varied. The bounds labeled "BBN" and "CMB and Matter Spectra" apply to the integral of the GW spectrum over the frequency range spanned by the corresponding lines.

sensitivity of LIGO (the S5 run, which began in November of 2005) is expected to improve the sensitivity by another factor 10× - 100×, while Advanced LIGO is expected to achieve sensitivities better by yet another factor 100× - 1000×, eventually reaching $10^{-9} - 10^{-8}$ for Ω_0. The uncertainty in the final reach of LIGO and of Advanced LIGO comes from the potential instrumental correlations that could be present between the collocated Hanford interferometers and from the uncertainty in the final optical configurations of interferometers in Advanced LIGO. The result discussed in this paper is still weaker than the indirect BBN bound, but the future runs by LIGO and Advanced LIGO are expected to surpass this bound.

The standard inflationary models are most stringently constrained by the CMB bound at lowest frequencies. Although they are most likely out of range of LIGO and of Advanced LIGO, they may be accessible to future GW interferometers (Smith et al. 2006b). However, there are models of stochastic GW background that LIGO is beginning to explore. We illustrate this with examples of cosmic string and pre-big-bang models.

4.2. Implications for Cosmic Strings Models

Cosmic strings can be formed as linear defects during symmetry breaking phase transitions in the early Universe as well as in string theory inspired inflation scenarios. In the latter case they have been dubbed cosmic superstrings. CMB data is not consistent with cosmic strings as the predominant source of density fluctuations in the Universe. Their existence, however, is not ruled out below the GUT scale and cosmic strings may still lead to a myriad of detectable astrophysical signatures such as gravitational radiation, gamma-ray bursts and ultra-high energy cosmic rays. For a review, see (Vilenkin & Shellard 2000).

(Damour & Vilenkin 2005) investigated the stochastic background of gravitational waves produced by cusps on cosmic strings, integrated over all redshifts and all directions on the sky. They find that three parameters define the gravitational-wave spectrum due to cosmic strings:

- String tension μ: This parameter is usually expressed as a dimensionless quantity $G\mu$ (assuming speed of light $c = 1$), where G is Newton's constant. String-theory inspired inflation scenarios prefer the range $10^{-11} \leq G\mu \leq 10^{-6}$.
- Reconection probability p: While ordinary, field-theoretic strings reconnect whenever they intersect ($p = 1$), the reconnection probability for superstrings is typically smaller than 1. In particular, the theoretically favored range is $10^{-3} \leq p \leq 1$ (Jackson et al. 2005).

- ϵ: This parameter describes the typical size of the closed loops produced in the string network. The value of this parameter is uncertain, and it can span several orders of magnitude. We will consider the range $10^{-13} < \epsilon < 10^{-2}$, which is both theoretically viable and most interesting from the point of view of LIGO.

These parameters determine both the amplitude and the shape of the gravitational-wave spectrum. In particular, parameters ϵ and $G\mu$ determine the lowest frequency (at a given redshift) at which a string loop could emit gravitational radiation. Since there is a low-frequency cut-off to the predicted gravitational-wave spectrum, it is possible to have a cosmic string model that would avoid the low-frequency bounds due to CMB or pulsar timing measurements, but still be within reach of LIGO (c.f. Figure 14).

Figure 15 shows the region of the parameter space (for $p = 10^{-3}$) excluded by the result discussed in this paper and by the S3 result (Abbott et al. 2005), as well as the expected reach of LIGO and Advanced LIGO in future runs. As shown in this Figure, LIGO is most sensitive to the regions of large $G\mu$ and small ϵ. Moreover, LIGO results are complementary to the pulsar timing limit, which is most sensitive to models with large $G\mu$ and large ϵ, and to the indirect BBN limit. In particular, the population of models with $p = 10^{-3}$, $\epsilon \lesssim 5 \times 10^{-11}$, and $5 \times 10^{-9} \lesssim G\mu \lesssim 7 \times 10^{-8}$ are excluded by the result discussed in this paper, but are not accessible to other current experimental bounds. To produce this Figure, we used Equations 4.1-4.7 from (Damour & Vilenkin 2005).

We note that as p increases toward 1, the bounds/reach of all experiments in the $G\mu - \epsilon$ plane weaken because the amplitude of the gravitational-wave spectrum scales with $1/p$. We also note that there are significant uncertainties in the calculation discussed by (Damour & Vilenkin 2005), mostly due to incomplete understanding of the string network behavior. For example, the size of loops is usually assumed to be given by the scale of gravitational back reaction. Recent numerical simulations of cosmic string networks (Martins & Shellard 2006), (Vanchurin et al. 2005), and (Ringeval et al. 2005) instead suggest that loop sizes are related to the large scale dynamics of the network. If this is the case then the expected stochastic background at the frequencies of pulsar timing experiments could be subtantially larger (Hogan 2006). Additionally, the treatment of (Damour & Vilenkin 2005) did not account for the effects of late-time acceleration. Thus a more detailed analysis of the stochastic background produced by cosmic strings is necessary.

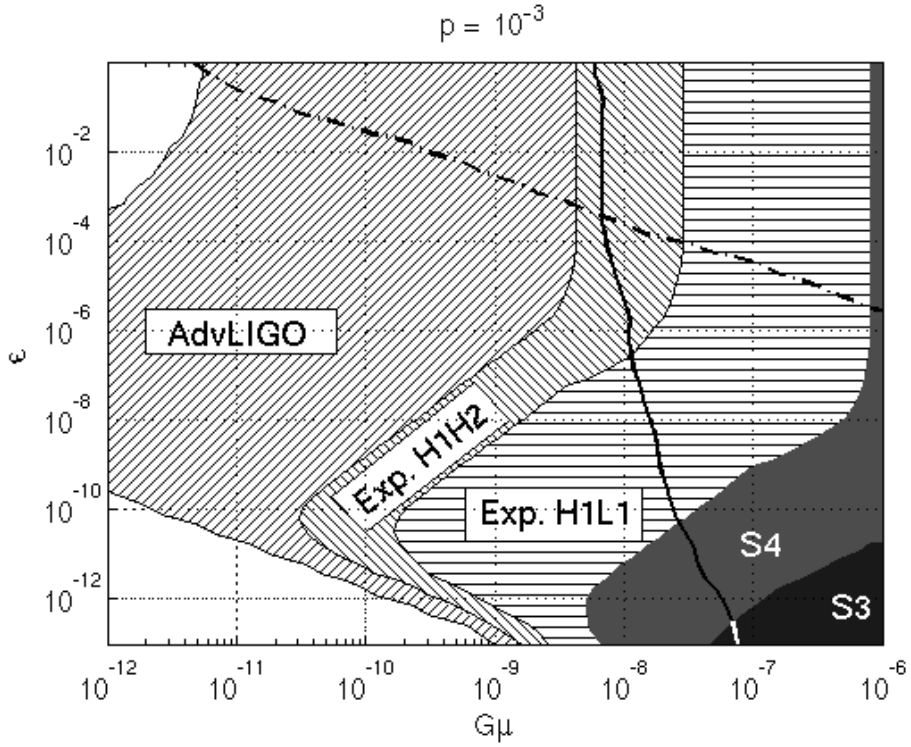

Fig. 15.— The ϵ - $G\mu$ plane for the cosmic string models with $p = 10^{-3}$. The shaded regions are excluded by the LIGO S3 limit (darker) and by the LIGO S4 limit presented here (lighter). The hatched regions are accessible to future LIGO runs: expected LIGO sensitivity for the H1L1 pair, assuming design interferometer strain sensitivity, and 1 year of exposure ('−'); expected LIGO sensitivity for the H1H2 pair, assuming design interferometer strain sensitivity, and 1 year of exposure ('\'); expected Advanced LIGO sensitivity for the H1H2 pair, assuming interferometer strain sensitivity tuned for the binary neutron star inspiral search and 1 year of exposure ('/'). The dash-dotted black curve is the exclusion curve based on the pulsar limit (Jenet et al. 2006) (the excluded region is above the curve). The solid black curve is the exclusion curve based on the indirect big-bang-nucleosynthesis bound (the excluded region is to the right of the curve).

4.3. Implications for Pre-Big-Bang Models

Pre-big-bang models are cosmology models motivated by string theory (Gasperini & Veneziano 1993), (Gasperini & Veneziano 2003). In these models, the Universe evolves through several phases: "dilaton" phase in which the Universe is large and shrinking; "stringy" phase in which the curvature of the Universe is high; and standard radiation and matter dominated phases. The GW spectrum is generated by amplification of vacuum fluctuations as the Universe transitions from one phase to another. The shape and amplitude of the spectrum are determined by the states of the Universe in the different phases. Although the "stringy phase" of the model and the transition to the radiation phase are not well understood, some models have been proposed in the literature that may partially describe it. In the formalism developed by (Buonanno et al. 1997), the GW spectrum produced by the model can be described as:

- $\Omega_{\rm GW}(f) \sim f^3$ for $f < f_s$, where f_s is essentially unconstrained.
- $\Omega_{\rm GW}(f) \sim f^{3-2\mu}$ for $f_s < f < f_1$, where $\mu < 1.5$ defines the evolution of the Universe in the "stringy" phase. The cutoff frequency f_1 is determined by string-related parameters and its most natural value is expected to be 4.3×10^{10} Hz.

Following the analysis in (Mandic & Buonanno 2006), we scan the parameter space (f_s, μ, f_1). For each set of values of these parameters, we calculate the GW spectrum following (Buonanno et al. 1997) and check whether the model is accessible to the current (and past) LIGO results. We also project the sensitivity of initial and Advanced LIGO to these models. Figure 16 shows the $f_1 - \mu$ plane for $f_s = 30$ Hz. Note that the LIGO S3 and S4 results are beginning to explore the parameter space of these models, although the indirect BBN bound is still a stronger constraint. Future runs of LIGO and of Advanced LIGO are expected to explore significantly larger parts of the parameter space, eventually surpassing the BBN bound (in some parts of the parameter space) and even reaching the most natural value of $f_1 = 4.3 \times 10^{10}$ Hz.

5. Conclusions

LIGO data acquired during the science run S4 yield a new Bayesian 90% upper limit on the amplitude of the stochastic GW background: $\Omega_0 < 6.5 \times 10^{-5}$ for the frequency-independent GW spectrum ($\alpha = 0$) in the frequency band 51-150 Hz. Similar limits are obtained for other values of α, as shown in Figure 11. This result is an improvement by a factor 13× over the previous upper limit in the same frequency range, obtained by LIGO in the science run S3.

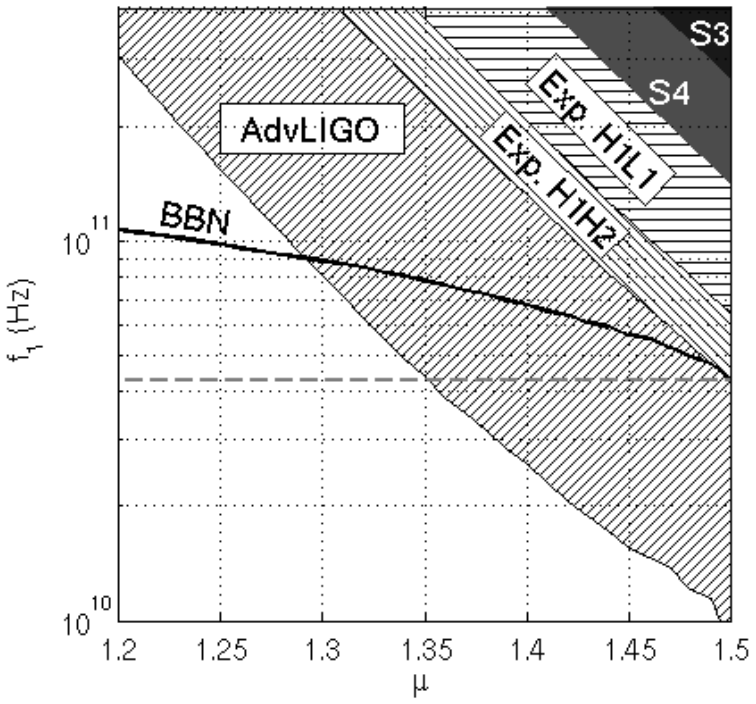

Fig. 16.— The $f_1 - \mu$ plane for the pre-big-bang models with $f_s = 30$ Hz. The shaded regions are excluded by the LIGO S3 limit (darker) and by the LIGO S4 limit presented here (lighter). The hatched regions are accessible to future LIGO runs: expected LIGO sensitivity for the H1L1 pair, assuming design interferometer strain sensitivity, and 1 year of exposure ('−'); expected LIGO sensitivity for the H1H2 pair, assuming design interferometer strain sensitivity, and 1 year of exposure ('\'); expected Advanced LIGO sensitivity for the H1H2 pair, assuming interferometer strain sensitivity tuned for the binary neutron star inspiral search and 1 year of exposure ('/'). The solid black curve is the exclusion curve based on the BBN limit (the excluded region is above the curve). The horizontal dashed line denotes the most natural value of $f_1 = 4.3 \times 10^{10}$ Hz.

This result is obtained using 192-sec long intervals of data with 1/32 Hz frequency resolution of the spectra, and it properly excludes the known instrumental correlations at 1 Hz harmonics. It is fully consistent with the blind result that uses 60-sec long intervals of data with 1/4 Hz frequency resolution, which is slightly contaminated by the instrumental 1 Hz harmonics. It is also more conservative than the blind result, as the theoretical error is larger due to the smaller amount of data available in the form of acceptable 192-sec intervals (as compared to the 60-sec intervals).

This result is complementary to the constraints on the gravitational-wave spectrum, based on the measurements of the CMB spectrum and pulsar timing. It is still weaker than the indirect BBN bound in the relevant frequency range. The ongoing 1-year long run of LIGO at the design sensitivity, and the future runs of Advanced LIGO, are expected to surpass the BBN bound. Furthermore, this result is already exploring the parameter space of some models of the stochastic GW background, such as cosmic strings models and pre-big-bang models.

The authors gratefully acknowledge the support of the United States National Science Foundation for the construction and operation of the LIGO Laboratory and the Particle Physics and Astronomy Research Council of the United Kingdom, the Max-Planck-Society and the State of Niedersachsen/Germany for support of the construction and operation of the GEO600 detector. The authors also gratefully acknowledge the support of the research by these agencies and by the Australian Research Council, the Natural Sciences and Engineering Research Council of Canada, the Council of Scientific and Industrial Research of India, the Department of Science and Technology of India, the Spanish Ministerio de Educacion y Ciencia, The National Aeronautics and Space Administration, the John Simon Guggenheim Foundation, the Alexander von Humboldt Foundation, the Leverhulme Trust, the David and Lucile Packard Foundation, the Research Corporation, and the Alfred P. Sloan Foundation. LIGO DCC number: P060012-06-D.

REFERENCES

Abbott B. et al. 2005, Phys. Rev. Lett. 95, 221101

Abbott B. et al. 2004a, Nucl. Instr. Meth. A 517, 154

Abbott B. et al. 2004b, Phys. Rev. D 69, 122004

Allen, B. 1996, preprint (gr-qc/9604033)

Allen, B. & Koranda, S. 1994, Phys. Rev. D 50, 3713

Allen, B., & Romano, J. 1999, Phys. Rev. D 59, 102001

Apreda, R., Maggiore, M., Nicolis, A., and Riotto, A. 2002, Nucl. Phys. B 631, 342

Armstrong, J.W. et al. 2003, Astrophys.J. 599, 806

Astone P. et al. 1999, Astron. Astrophys. 351, 811

Baskaran, D., Grishchuk, L.P., and Polnarev, A.G. 2006, gr-qc/0605100.

Bendat, J.S. and Piersol, A.G. 2000, *Random Data Analysis and Measurement Procedures*, (John Wiley & Sons, Inc., New York, NY)

Bennet, C.L. et al. 2003, Astrophys. J. Suppl. 148, 1

Bose, S. et al. 2003, Class. Quant. Grav. 20, S677

Buonanno, A., Maggiore, M., and Ungarelli, C. 1997, Phys. Rev. D 55, 3330

Caldwell, R.R. & Allen, B. 1992, Phys. Rev. D 45, 3447

Cooray, A. 2004, Mon. Not. R. Astron. Soc. 354, 25

Coward, D.M., Burman, R.R. and Blair, D.G. 2002, Mon. Not. R. Astron. Soc. 329, 411

Cyburt, R.H., Fields, B.D, Olive, K.A., and Skillman, E. 2005, Astropart. Phys. 23, 313

Damour, T. & Vilenkin, A. 2000, Phys. Rev. Lett. 85, 3761

Damour, T. & Vilenkin A. 2005, Phys. Rev. D 71, 063510

Fotopoulos, N. 2006, Class. Quantum Grav. (in press)

Gasperini, M. & Veneziano, G. 1993, Astropart. Phys. 1, 317

Gasperini, M. & Veneziano, G. 2003, Phys. Rep. 373, 1

Grishchuk, L.P. 1975, Sov. Phys. JETP 40, 409

Grishchuk, L.P. 1997, Class. Quantum Grav., 14, 1445

Hogan, C.J., astro-ph/0605567

Jackson, M.G., Jones, N.T., and Polchinski, J. 2005, JHEP 0510, 013

Jenet, F.A. et al. 2006, astro-ph/0609013 (to appear in Astrophys. J.)

Kolb, E. & Turner, R. 1990, *The Early Universe*, (Addison-Wesley, Reading, MA)

Kosowsky, A., Turner, M.S., and Watkins, R.1992, Phys. Rev. Lett. 69, 2026

Loredo, T.J. 1990, in *Maximum Entropy and Bayesian Methods*, edited by P. F. Fougère (Kluwer Academic, Dordrecht, 1990)

Lazzarini, A., & Romano, J. 2004, LIGO preprint, http://www.ligo.caltech.edu/docs/T/T040089-00.pdf

Maggiore, M. 2000, Phys. Rep. 331, 283

Mandic, V. & Buonanno, A. 2006, Phys. Rev. D 73, 063008

Martins, C.J.A.P. and Shellard, E.P.S. 2006, Phys. Rev. D 73, 043515

Regimbau, T. & de Freitas Pacheco, J.A. 2001, Astron. and Astrophys. 376, 381

Ringeval, C., Sakellariadou, M. and Bouchet, F., astro-ph/0511646

Smith, T.L. et al. 2006a, astro-ph/0603144

Smith, T.L. et al. 2006b, Phys. Rev. D 73, 123503

Starobinsky, A.A. 1979, Pis'ma Zh. Eksp. Teor. Fiz. 30, 719

Turner, M.S. 1997, Phys. Rev. D 55, R435

Vanchurin, V., Olum, K.D. and Vilenkin, A., gr-qc/0511159

Vilenkin, A. & Shellard, E.P.S. 2000, *Cosmic Strings and Other Topological Defects*, (Cambridge University Press, Cambridge, MA)

This preprint was prepared with the AAS LaTeX macros v5.2.